ADVANCED MATERIALS TECHNOLOGIES
www.advmattechnol.de

A Unified Enhanced Quasi-Electrostatic 3D Charge Model for Accurate Prediction and Design Optimization of Contact–Separation Triboelectric Nanogenerators

Seokjin Kim, Jang–Woo Han, and Jihoon Chung**

An integrated theoretical model for a vertical contact– and separation– mode triboelectric nanogenerator (VCS–TENG) is presented to improve the accuracy of electrostatic behavior predictions and forecast its electrical output characteristics more effectively. Existing theoretical models for VCS–TENG are reviewed and unified to develop a new model. The formulation used to evaluate the electric potential difference is modified, and a mathematical technique is introduced for simplification. The newly derived model is validated by comparing it with experimental results. Moreover, the effects of various parameters on the electrical output characteristics are investigated using theoretical and experimental methods, and similar trends are observed. This new theoretical model can be used to predict VCS–TENG output performance and optimize its structural design.

1. Introduction

Maxwell's equations provide the fundamental frameworks for classical electrodynamics, with displacement current enabling the theoretical conversion of mechanical energy into electrical energy.[1] The triboelectric nanogenerator (TENG), pioneered by Wang in 2012,[2] is an innovative technology that harvests ambient random movements based on Maxwell's displacement current.[3] Since the introduction of TENG, extensive research has contributed to elevating their output performance through material selection,[4–6] mechanical design,[7–9] power management,[10–12] and coupling effect with other technologies.[13] Furthermore, many studies have reported that TENG has the potential for practical applications such as purification,[14,15] sensing,[16,17] and energy harvesting.[18–20] TENG is expected to have promising applications in micro/nano power sources, self–powered sensing, high–voltage power sources, and electrical stimulation.[21]

Previous studies established a fundamental framework describing their electrostatic behavior and developed theoretical models to analyze the effects of the structural design on output characteristics. The first theoretical model is the capacitive (CA) model,[22] which employs the parallel-plate capacitor theory to explain a vertical contact- and separation-mode triboelectric nanogenerator (VCS–TENG). In this model, infinitely large, uniformly charged planes are introduced; therefore, it is concluded that the electric fields are constant with distance and are perpendicular to the plates. Several years later, a distance-dependent electric field (DDEF) model for the VCS–TENG was introduced,[23] arguing that the uniformly distributed electric field concept is incorrect. By accounting for the lateral size of the charged plate, the DDEF model presents a more sophisticated formulation for evaluating the electric potential. Accordingly, the magnitude of the electric field depends on the distance from the charged plate. Moreover, the open–circuit voltage improved with increasing separation distance, accompanied by a decreasing gradient, whereas it was linearly proportional to the separation distance in the CA model. Although the DDEF model constructed more complicated theoretical explanations and aligned well with the experimental outcomes, the model was found to have two theoretical limitations. First, the formula derived from the DDEF model overestimates the electric potential because it considers only the distance dependence of the electric field along the central axis, without considering the 3D electric field distribution. The quasi–electrostatic 3D (QETD) charge model addresses this issue,[24] but it demands the evaluation of multiple integrals that are too difficult to conduct analytically or numerically. Another limitation is that although the DDEF model considers the 3D distribution of charges, it is not reduced to the CA model when the separation distance is so small that the parallel–plate capacitor assumption can be accepted. An enhanced distance–dependent electric field (EDDEF) model[25] was introduced to address this problem. However, no model has simultaneously addressed both limitations. Therefore, an alternative theoretical method should be developed to overcome mathematical complexities and accurately portray the electric field distribution.

S. Kim, J. Han, J. Chung
School of Mechanical System Engineering
Kumoh National Institute of Technology
61 Daehak–ro, Gumi–si, Gyeongsangbuk–do 39177, Republic of Korea
E-mail: uddan@kumoh.ac.kr; jihoon@kumoh.ac.kr

The ORCID identification number(s) for the author(s) of this article can be found under https://doi.org/10.1002/admt.202500401

DOI: 10.1002/admt.202500401

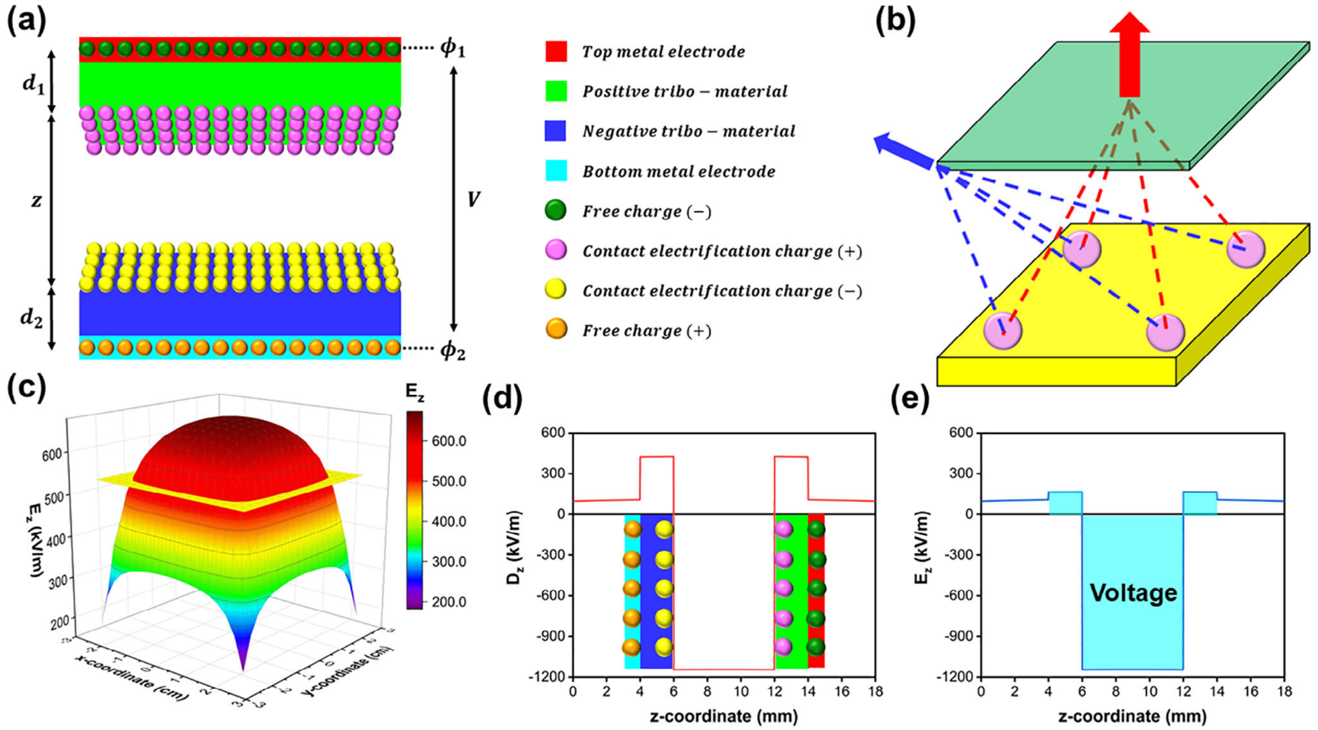

Figure 1. Graphical overview of derivation background of the EQETD model. a) The schematic illustration of the dielectric–dielectric VCS–TENG. d_1 and d_2 are the thicknesses of the positive and negative tribomaterials, z is the air gap thickness between tribomaterials, ϕ_1 and ϕ_2 are the electric potentials on the electrodes attached to the positive and negative tribomaterials, respectively. V represents the electric potential difference between the electrodes, which is defined as: $V = \phi_1 - \phi_2$. b) Electric field vector at the center and corner of the plate created by finitely discretized charges that are spatially distributed. c) A diagram of spatially variant electric field component created by continuously distributed charges. The yellow plane represents the average electric field strength of the electric field distribution. d) Electric displacement component with respect to z–coordinate. e) Electric field component with respect to z–coordinate. The voltage is equal to the painted area enclosed by an electric field component curve and both electrodes.

In this study, we propose an enhanced quasi–electrostatic 3D (EQETD) charge model, which is a hybrid model combining the QETD and EDDEF models. We simultaneously corrected two limitations, as mentioned in previous studies, by utilizing the methods they presented. Additionally, to overcome the problem of multiple integrals being calculated, Coulomb's law and Gaussian Quadrature were utilized as mathematical techniques,[26,27] which reduce multiple integrals into the summation of double integrals. The derived model showed a better correlation with the experimental results than existing models. It can be used to predict the output characteristics of VCS–TENG more accurately and optimize its structural design more efficiently.

2. Quantitative Explanation of the Existing and Proposed Theoretical Model for VCS–TENG

2.1. Device Structure and Working Mechanism of VCS–TENG

See **Figure 1a** for an example of VCS–TENG. When two dielectrics are in contact, a charge–transfer phenomenon known as contact electrification occurs between the interfaces.[28] One surface loses electrons and becomes positively charged, whereas the other gains electrons and becomes negatively charged. The former is referred to as a positive tribomaterial, and the latter as a negative tribomaterial. Once the charge is transferred, it remains bound for an extended period, even when the contact no longer continues. Electrostatic induction plays a crucial role in transferring charge between electrodes.[28] As the two dielectrics move away from each other, the electric potential difference between the electrodes increases. When they are connected through an external circuit, electrons flow from the negatively induced electrode to the positively induced one. In this illustration, the top electrode was positively induced, whereas the bottom electrode was negatively induced, causing electrons to flow from the bottom to top electrode. Consequently, the top electrode becomes negatively charged, whereas the bottom electrode becomes positively charged by the transferred electrons.

2.2. Discussion of the Background and Limitations of Each Model for VCS–TENG

In this section, we abbreviate infinite plane and finite plate as "plane" and "plate", respectively. Gauss's theorem proves that a uniformly charged plane creates uniform electric fields.[26] Inspired by this point, the CA model approximates the electric field around the TENG to be spatially invariant although it has finite dimensions.[22] This approximation is reasonable only if the region of interest is close to the charge. Thus, assuming that charged plates are placed facing each other, the CA model presents a good approximation of the electric field around the TENG at small separation distances. To evaluate the electric field at a point far away from the charged plate, it is more reasonable to approximate the charged plate as a point charge than a plane charge. Therefore, the prediction of the CA model becomes inaccurate when the charged plate is laterally slid or vertically separated far apart. To address this issue, the DDEF model considered the electric field created by not a plane but a plate.[23] The major differences between the DDEF and CA models are as follows: First, the magnitude of the electric field predicted by the DDEF model is lower than that predicted by the CA model because the amount of charge contributing to the formation of the electric field is reduced. Second, the variation of the electric field with respect to the separation distance calculated from the DDEF model decreases with distance while the other remains constant with distance because the electric field created by a charged plate behaves like that created by a point charge under a region far apart from the charge. Thus, the DDEF model is a more generalized theory capable of being applied to the case where the plates are separated from far away. A few years later, two limitations of the DDEF model were identified and modified by the QETD and EDDEF models, respectively. Both limitations are related to the electric potential difference between the two electrodes, defined as "voltage", which is evaluated by integrating the electric field along a straight line perpendicular to the plate, defined as "path". One of the limitations is an overestimation issue of the voltage.[24] The DDEF model chooses the central line of the plate as the integration path. However, the calculated voltage is dependent on the path selection because the electric field is spatially variable even when the height of the point of interest from the plate is kept constant. The path independence in this context is not consistent with the definition from calculus. In calculus, path independence means that the integration of a function along the path is constant even when the path is varied only if the initial and final points of the path are fixed. In the case of the theoretical model for VCS–TENG, the path itself determines both end points because the path is aligned to be perpendicular to the plate. The calculated voltage is maximized when the central axis is chosen as the path, and the value may be different when another path is considered. The QETD model pointed out the inaccuracy of the previous method and proposed a modified approach to evaluate the voltage, which averages the voltage obtained from each path over the plate. The predicted voltage from the QETD model is slightly lower than that from the DDEF model. The other limitation is a discrepancy in the voltage predicted from different models.[25] As mentioned above, the CA model presents a good approximation of the electric field when the plates are facing each other with a small gap. Hence, it is expected for similar trends to be predicted when utilizing the other theoretical model in this condition. However, the DDEF model predicts a deviated tendency from that of the CA model even when the separation distance is so small that the plane charge assumption is valid. This observation implies that the DDEF model approximates the electric field around the charged plate inaccurately. To be specific, the error results from the selection of the integration path during the evaluation of the voltage. The DDEF model takes a central line of the plate from the infinity point to the electrode as a path. Similarly, the QETD model takes a bundle of straight lines from the infinity points to the electrode as paths. However, these approaches contradict that of the CA model, which takes a central line of the plate connecting the two electrodes as the path. The EDDEF model proposed a modified method to evaluate the voltage exploiting the electric field predicted from the DDEF model and the integration path introduced from the CA model. Consequently, the voltage calculated from the EDDEF model converges to that of the CA model at small separation distances and behaves with distance like that of the DDEF model at large separation distances.

2.3. Derivation Concept and Graphical Description of the EQETD Model for a VCS–TENG

Figure 1b–e graphically describes what issues the QETD and EDDEF models treated and how the models are integrated into the EQETD model. Figure 1b shows a charged plate and the electric field created around the plate. An electric field vector created by a few charged particles can be evaluated with Columb's law and superposition principle.[26] Through a simple calculation, it can be proved that the electric field at the center is perpendicular to the plate and be maximized while the electric field at the corner is inclined to the plate and its normal component to the plate is smaller than that of the preceding case. For more details, Figure 1c provides the numerical computation results about the spatially distributed normal component of the electric field to the plate created by the spatially distributed charges. As shown in the Figure, the electric field component is maximized at the center and decreased as being apart from the center. Therefore, considering only the electric field at the center results in overestimation of the electric field distribution. To correct this error, the QETD model proposed the method approximating the electric field distribution by averaging those. The averaged distribution over the plate is illustrated in Figure 1c as the yellow plane. Figure 1d,e shows the normal component of an electric displacement vector to the plate and corresponding electric field component as a function of z–coordinate, respectively. As mentioned earlier, the EDDEF model evaluated the voltage by integrating the electric field at the center along the central axis between both electrodes. This feature is well captured in Figure 1e. The painted area is equal to the voltage. Now we unite the QETD and EDDEF models by numerically integrating the average electric field over the plate as shown in Figure 1c along z–coordinate between the electrodes as shown in Figure 1e.

2.4. Assumed Conditions for Deriving the New Theoretical Model for a VCS–TENG and the Possibilities for the New Model to be Extend to other Working Modes of TENG

We assumed a few ideal conditions to simplify the derivation process and results of the new theoretical model for a VCS–TENG even though they cannot be satisfied strictly under practical circumstances. First, we assume that the variation of any quantity with respect to time is so slow that electrodynamics can be approximated by either quasi–electrostatics or quasi–magnetostatics. Under this assumption, the interaction between electric and magnetic fields becomes uncoupled, and only electric fields are to be considered in our problem. In general, the dielectric property of material is dependent on the position and orientation of the frame under study. Second, we assume that dielectric property is homogeneous and isotropic throughout the material. Under the two assumptions above, Maxwell's equation reduces to Poisson's equation with boundary conditions.[26] Poisson's equation can be solved analytically in terms of prescribed charge distribution exploiting the Green's third identities and boundary conditions are automatically dropped out if the dielectric constant of material is spatially invariant throughout space.[26] Third, we utilize this analytic solution to evaluate the electric potential even though the dielectric constant of material varies with the position of point under study. Because free electrons belonging to conductors become rearranged to achieve the electrostatic equilibrium when they are under external applied electric field, induced charge density cannot be prescribed and should be determined considering equilibrium conditions.[26] Fourth, we assume that induced charge density is uniform throughout the metal electrode. Then, the total induced charge amount is only remaining unknown. Arbitrary species of charges including electrons and ions can be transported by diffusion and drift mechanism. Accordingly, the charges on metal electrodes and tribo–materials can penetrate dielectric material or dissipate into the air.[29,30] Fifth, we disregard the transport mechanism and neglect the existence of charges in the air and the dielectric materials. Thus, only induced charge in metal electrodes and contact electrification charge in tribo–materials are considered. Dielectric breakdown is another charge transfer mechanism that proceeds momentarily due to high electric field condition.[25,31,32] Sixth, we also ignore this charge transfer phenomenon. Contact electrification does not ensure that generated charge is uniformly distributed throughout the contact interface. Seventh, we assume that contact electrification charge density is uniform. Periodic contact and separation between the interfaces of tribo–materials may lead to time accumulated contact electrification charge until they are saturated.[30] Eighth, we assume that contact electrification charge is in their steady state and invariant with time.[33] To make VCS–TENG generate electricity, relative movement between the two parts consisting of the TENG is required. The motion of objects is governed by Newton's second law, and net force acting on the body should comprise electrostatic force, which makes the analysis complicated. Nineth, we constrain the motion of the body of the TENG by specifying the displacement as function of time. Thus, electromechanical coupling effects are neglected.

It is worth noting what range this model can be extended to. The EQETD model was derived from a VCS–TENG. Therefore, this model cannot be directly applied to other TENG modes without additional considerations. However, the voltage evaluating approach suggested in this model might be extended to the theoretical analysis of TENG operating on other modes. Let us discuss this theme. As mentioned above, we supposed that the induced charge density is uniform throughout the electrode. This assumption was validated by previously published models for VCS–TENG,[22–25] which exploited the condition and provided reasonable outcomes in common. Thus, it is expected that the EQETD model could be extended to TENG operating on other modes if the assumption is still satisfied. For example, some papers theoretically analyzed vertical single–electrode mode TENG (VSE–TENG) and vertical freestanding mode TENG (VFS–TENG) assuming the uniformity condition of induced charge and verified the analysis with either comparison to other works or experiments.[34,35] In these cases, the EQETD model could be extended to modeling those, and we leave it for future studies. On the other hand, violence of the assumption may result in significant inaccuracy in model. To be specific, the induced charge may be distributed unevenly unless the two electrodes are facing each other. Representatively, a theoretical model for lateral sliding mode TENG (LS–TENG) assumed stepped variation on induced charge distribution and validated the model with both Finite Element Method (FEM) simulation results and experiments.[36] The EQETD model cannot be extended to this type of TENG. To address this TENG, theoretical models for themselves should be introduced, or numerical computations such as the FEM simulation should be utilized.

3. Mathematical Derivation of the New Theoretical Model for VCS–TENG

The current theoretical model for the VCS–TENG is compared and discussed in Notes S1–S5 (Supporting Information) in a mathematical sense. In this section, the mathematical expression of the new theoretical model for the VCS–TENG is presented. A detailed derivation of the formula is provided in Notes S6–S10 (Supporting Information). The results for the dielectric–dielectric VCS–TENG are introduced in this paper, while an explanation for the dielectric–metal VCS–TENG is provided in Note S11 (Supporting Information). The discussion begins by exploring a formula to evaluate the electric potential difference.

3.1. Electric Potential Difference

In the situation described in Figure 1a, the voltage (Note that the term "voltage" is defined as the electric potential difference between the two electrodes.) created by the four charged plates can be evaluated by the following process (see Notes S6–S10, Supporting Information for the detailed derivation process). First, we defined the following function:

$$f\left(x',\, y',\, z\right) = \int_{-\frac{W}{2}}^{\frac{W}{2}} \int_{-\frac{L}{2}}^{\frac{L}{2}} \left\{ \frac{1}{\left\{ \left(x'-a\right)^2 + \left(y'-b\right)^2 + z^2 \right\}^{\frac{1}{2}}} \right\} da\,db \tag{1}$$

where L and W represent the length and width of the plates, respectively. Next, define the following function.

$$M\left(z\right) = \frac{1}{16\pi} \sum_{j=1}^{n} \sum_{i=1}^{n} f\left(\frac{L}{2}u_i,\, \frac{W}{2}v_j,\, z\right) w_i w_j \tag{2}$$

where u_i and v_j are Gauss points, and w_i and w_j are Gauss weights. where n is the number of Gauss points and is a user–defined parameter.[27] The voltage was evaluated in terms of the separation distance, z.

$$\phi_1 - \phi_2 = -\sigma_c \left\{ \frac{\left[M\left(z\right)\right]_{d_1}^{0}}{\varepsilon_1} + \frac{\left[M\left(z\right)\right]_{d_1+z}^{d_1}}{\varepsilon_0} + \frac{\left[M\left(z\right)\right]_{d_1+z+d_2}^{d_1+z}}{\varepsilon_2} \right\} +$$

$$\sigma_t \left\{ \frac{[M(z)]_0^{d_1}}{\varepsilon_1} + \frac{[M(z)]_z^{0}}{\varepsilon_0} + \frac{[M(z)]_{z+d_2}^{z}}{\varepsilon_2} \right\} - \sigma_t \left\{ \frac{[M(z)]_z^{d_1+z}}{\varepsilon_1} + \frac{[M(z)]_0^{z}}{\varepsilon_0} + \frac{[M(z)]_{d_2}^{0}}{\varepsilon_2} \right\} + \sigma_c \left\{ \frac{[M(z)]_{z+d_2}^{d_1+z+d_2}}{\varepsilon_1} + \frac{[M(z)]_{d_2}^{z+d_2}}{\varepsilon_0} + \frac{[M(z)]_0^{d_2}}{\varepsilon_2} \right\} \tag{3}$$

where ϵ_1 and ϵ_2 are the permittivity of the positive and negative tribomaterials, respectively, ϵ_0 is the permittivity of the free space, σ_t is the contact electrification charge density of the positive tribomaterial, and σ_c is the induced charge density of the bottom electrode.

3.2. Short–Circuit Charge

Under short–circuit (SC) conditions, it is assumed that all the electrodes have an equal electric potential by transferring free charges between them. Thus, in the case above, $\phi_1 - \phi_2 = 0$ is satisfied and the induced charge density can be determined in terms of the separation distance, z.

$$\sigma_{c,\,SC}(z) = \sigma_t \frac{\left\{ \frac{[M(z)]_0^{d_1}}{\varepsilon_1} + \frac{[M(z)]_z^{0}}{\varepsilon_0} + \frac{[M(z)]_{z+d_2}^{z}}{\varepsilon_2} \right\} - \left\{ \frac{[M(z)]_z^{d_1+z}}{\varepsilon_1} + \frac{[M(z)]_0^{z}}{\varepsilon_0} + \frac{[M(z)]_{d_2}^{0}}{\varepsilon_2} \right\}}{\left\{ \frac{[M(z)]_{d_1}^{0}}{\varepsilon_1} + \frac{[M(z)]_{d_1+z}^{d_1}}{\varepsilon_0} + \frac{[M(z)]_{d_1+z+d_2}^{d_1+z}}{\varepsilon_2} \right\} - \left\{ \frac{[M(z)]_{z+d_2}^{d_1+z+d_2}}{\varepsilon_1} + \frac{[M(z)]_{d_2}^{z+d_2}}{\varepsilon_0} + \frac{[M(z)]_0^{d_2}}{\varepsilon_2} \right\}} \tag{4}$$

The determination of the induced charge density requires attention, as it depends on the charge reference state.[37] In this study, the minimum achievable charge reference state (MACRS) was used to evaluate the amount of charge transfer.[37] Accordingly, the amount of charge transferred between the electrodes under SC conditions is defined as follows:

$$Q_{SC,\,transferred}(z) = S\left\{\sigma_{c,\,SC}(z) - \sigma_{c,\,SC}(z_{min})\right\} \tag{5}$$

where z_{min} is the minimum separation distance z, and S is the area of the plate ($S = L \times W$). If the separation distance z is provided as a function of time t, the short–circuit current (I_{SC}) which is defined as the derivative of the amount of charge transferred with respect to time under the SC condition, is evaluated as follows:

$$I_{SC}(t) = \frac{d}{dt}\left\{Q_{SC,\,transferred}(z(t))\right\} = S\frac{d}{dt}\left\{\sigma_{c,\,SC}(z(t))\right\} \tag{6}$$

3.3. Open–Circuit Voltage

Under open–circuit (OC) conditions, it is assumed that charge transfer between the electrodes is not allowed. Therefore, even when the separation distance z varies, the induced charge density remains constant, which is the value obtained when $z = z_{min}$.

$$\sigma_c = constant = \sigma_{c,\,SC}(z_{min}) \tag{7}$$

The voltage under OC conditions is evaluated by substituting Equation (7) into Equation (3).

$$V_{OC}(z) = -\sigma_{c,\,SC}(z_{min}) \left\{ \frac{[M(z)]_{d_1}^{0}}{\varepsilon_1} + \frac{[M(z)]_{d_1+z}^{d_1}}{\varepsilon_0} + \frac{[M(z)]_{d_1+z+d_2}^{d_1+z}}{\varepsilon_2} \right\} + \sigma_t \left\{ \frac{[M(z)]_0^{d_1}}{\varepsilon_1} + \frac{[M(z)]_z^{0}}{\varepsilon_0} + \frac{[M(z)]_{z+d_2}^{z}}{\varepsilon_2} \right\} - \sigma_t \left\{ \frac{[M(z)]_z^{d_1+z}}{\varepsilon_1} + \frac{[M(z)]_0^{z}}{\varepsilon_0} + \frac{[M(z)]_{d_2}^{0}}{\varepsilon_2} \right\} + \sigma_{c,\,SC}(z_{min}) \left\{ \frac{[M(z)]_{z+d_2}^{d_1+z+d_2}}{\varepsilon_1} + \frac{[M(z)]_{d_2}^{z+d_2}}{\varepsilon_0} + \frac{[M(z)]_0^{d_2}}{\varepsilon_2} \right\} \tag{8}$$

where V denotes the voltage.

$$V = \phi_1 - \phi_2 \tag{9}$$

3.4. Capacitance

The capacity of an electrostatic system is defined as the amount of charge accumulated at each electrode divided by the electric potential difference between the electrodes.[26] For a TENG, capacitance is evaluated as the ratio of charge transferred between the electrodes under SC conditions to the electric potential difference under OC conditions,[38] mathematically expressed as:

$$C(z) = \frac{Q_{SC,\,transferred}(z)}{V_{OC}(z)} \tag{10}$$

3.5. Power Dissipation Through Load Resistors

The simplest external circuit configuration of a TENG is a resistive connection between the electrodes. Under this condition, based on Ohm's law, the relationship between voltage and induced charge density is expressed as follows:

$$V = RS\frac{d\sigma_c}{dt} \tag{11}$$

where R is the resistance of the external resistive connections. The power dissipation P through the load resistor R is evaluated as follows:

$$P = \frac{V^2}{R} = R\left(S\frac{d\sigma_c}{dt}\right)^2 \tag{12}$$

3.6. The Governing Equation of the TENG

By combining Equation (3) and Equation (11), the governing equation of the TENG is derived as follows:

$$RS\frac{d\sigma_c}{dt} = -\sigma_c \left\{ \frac{[M(z)]_{d_1}^{0}}{\varepsilon_1} + \frac{[M(z)]_{d_1+z}^{d_1}}{\varepsilon_0} + \frac{[M(z)]_{d_1+z+d_2}^{d_1+z}}{\varepsilon_2} \right\} +$$

$$\sigma_t \left\{ \frac{[M(z)]_0^{d_1}}{\varepsilon_1} + \frac{[M(z)]_z^{0}}{\varepsilon_0} + \frac{[M(z)]_{z+d_2}^{z}}{\varepsilon_2} \right\} - \sigma_t \left\{ \frac{[M(z)]_z^{d_1+z}}{\varepsilon_1} + \frac{[M(z)]_0^{z}}{\varepsilon_0} + \frac{[M(z)]_{d_2}^{0}}{\varepsilon_2} \right\} + \sigma_c \left\{ \frac{[M(z)]_{z+d_2}^{d_1+z+d_2}}{\varepsilon_1} + \frac{[M(z)]_{d_2}^{z+d_2}}{\varepsilon_0} + \frac{[M(z)]_0^{d_2}}{\varepsilon_2} \right\} \quad (13)$$

This is a first–order ordinary differential equation (ODE) with respect to the variable t. If the separation distance z is provided as a function of t, this ODE can be solved in terms of σ_c. Conventionally, z is defined as sinusoidal movement with respect to t, and we followed this rule as well.

3.7. Energy Conversion Efficiency in the TENG

According to a previous work that covers the energy conversion in TENG,[39] the ratio η between the output electrical energy E_{out} and the effective input mechanical energy $E_{in,\,eff}$ per cycle is defined as the single–cycle energy conversion efficiency, which is given by:

$$\eta = \frac{\oint VdQ}{\oint Fdx|Fdx \geq 0} \quad (14)$$

where the symbol F is utilized to express the minimum–required input force to overcome the electrostatic force. We derived the mathematical expression for the F in Note S13 (Supporting Information), and rewrite that here once again.

$$F = \frac{\sigma_c\sigma_c}{2}\frac{\partial}{\partial z}\left[G_{cc}(z)\right] + \frac{\sigma_c\sigma_t}{2}\frac{\partial}{\partial z}\left[G_{ct}(z)\right] + \frac{\sigma_t\sigma_t}{2}\frac{\partial}{\partial z}\left[G_{tt}(z)\right] \quad (15)$$

E_{out} can be simply calculated by integrating the instantaneous power evaluated through Equation (12) with respect to the time during one cycle. $E_{in,\,eff}$ is calculated by integrating the work done by mechanical input force during one cycle. The expression $Fdx \geq 0$ means that only positive work is considered in integration because the negative work made will be dissipated as the heat energy.

4. Results and Discussion

To investigate the effects of certain parameters on output characteristics, theoretical simulations were conducted using the EQETD model. Experiments validated the proposed theoretical model. Detailed experimental methods and parameters are provided in the Experimental Section and Table S1 (Supporting Information).

4.1. Electrostatic and Electrical Output Characteristics under Ideal Loading Conditions

The open–circuit voltage (V_{OC}), short–circuit charge (Q_{SC}), and capacitance (C) as functions of the separation distance are key indicators of the output performance under practical load resistor conditions. To explore this, theoretical simulations were conducted using the EQETD model, as shown in **Figure** 2a–c. V_{OC} increases with distance and eventually stabilizes. This trend agrees with that predicted from existing quasi–electrostatic models,[23–25] as both the new and prior models are derived from the DDEF concept. In practical applications, where free charges are allowed to flow between electrodes, the voltage is neutralized by induced charges and is always lower than V_{OC}. Like V_{OC}, Q_{SC} also increases and eventually reaches a plateau with distance. This implies that the amount of charge transferred has an upper limit. This behavior is consistent with all existing models, including the capacitive and quasi–electrostatic models.[22–25] In contrast, the capacitance diminishes with distance, which is defined as the ratio of Q_{SC} to V_{OC}. This is the main factor used to evaluate electrical output in the basic TENG equation.[38] V_{OC}, Q_{SC}, and I_{SC} were evaluated as functions of time, with separation distance modeled as a sinusoidal movement with respect to time, as shown in Figure 2d–f. These simulations showed peak value of V_{OC}, Q_{SC}, and I_{SC} as 7 kV, 29.7 nC, and 0.72 µA, respectively. These results confirm that the TENG is an electrical power source that features high voltage and low current.[3]

4.2. Electrical Output Characteristics under Different Realistic Load Resistors

The effect of external load resistance on the output characteristics was explored theoretically. To simulate the dynamic characteristics of the VCS–TENG, Equation (13) was solved assuming that the accumulated charge in the initial state was zero. **Figure 3** depicts the behaviors of the output charge, current, and voltage under different external load resistance conditions. We selected 10 MΩ, 100 GΩ, and ∞ Ω of resistance as usual circuit condition, remarkably high loading condition, and ideal OC condition, respectively. As shown in the Figure, the electrical output profile varies significantly with resistance. Under the lowest resistance conditions shown in Figure 3a, the output charge experiences both its minimum and maximum peaks within one cycle. This indicates that charge transfer between the electrodes is minimally hindered and occurs readily. Similarly, the output current and voltage have already been fully developed since the initial state and remain constant over time. These tendencies are typically observed in electrical experiments involving TENG devices. The output characteristics under medium resistance conditions are shown in Figure 3b. In this case, the output has a transient state followed by a steady state. The output charge starts at zero in the initial state, steadily increases, and eventually stabilizes around a specific value. The corresponding output current and voltage behaves as underdamped vibrating oscillators. They exhibited a maximum peak within the first cycle, and the values of the following peaks decreased exponentially and ultimately remained constant. These trends are explained as follows. In the initial state, the charge captured at the electrodes is zero, so the contact electrification charges play a dominant role in creating an electric potential. This electric potential causes the electrons to flow between the electrodes, thereby neutralizing the charges. Over time, a significant charge accumulates at the electrodes, which is comparable to the contact electrification charge.

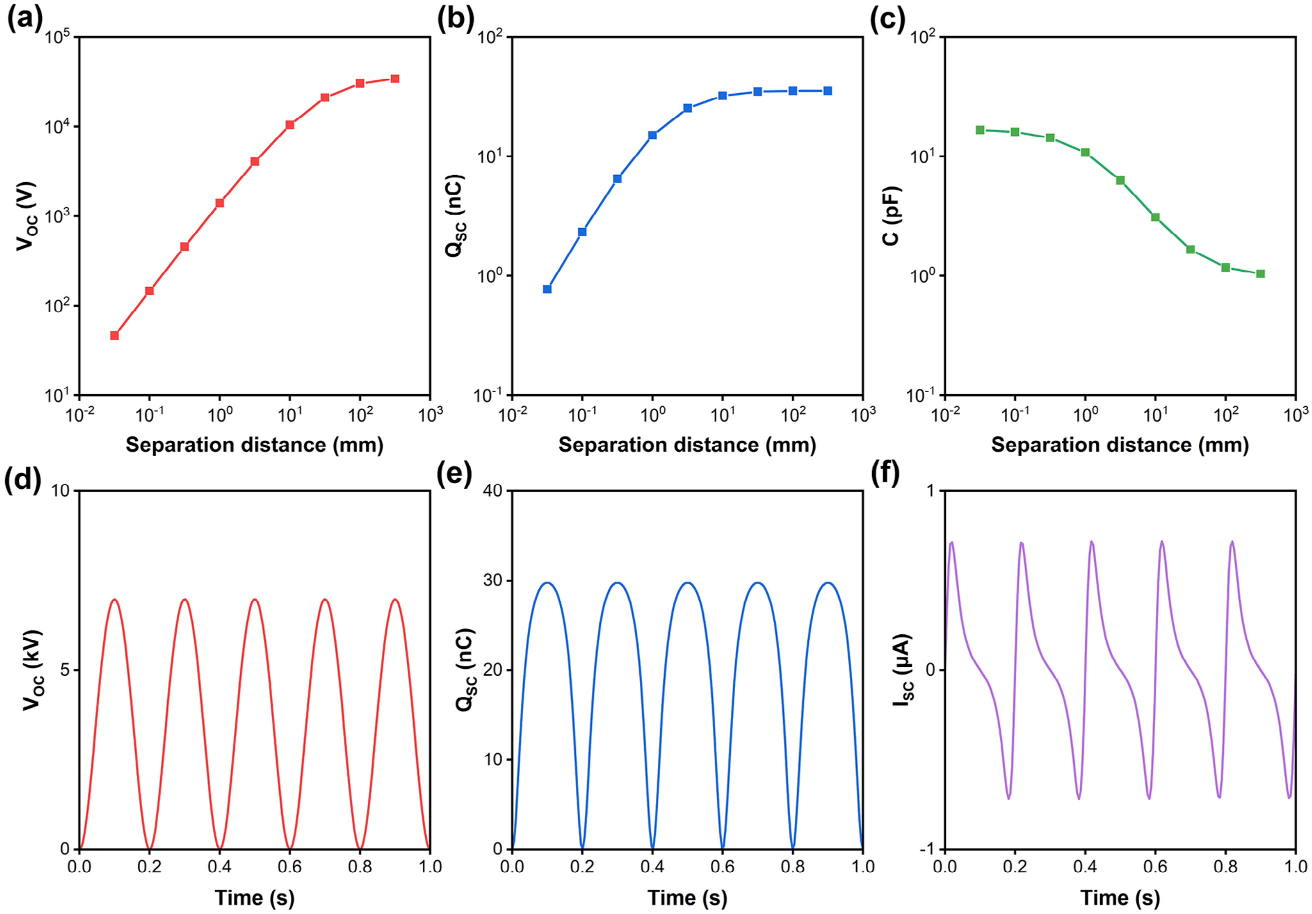

Figure 2. Theoretical simulation for ideal loading conditions, including OC and SC conditions. a) V_{OC}, b) Q_{SC}, and c) C versus separation distance in logarithm scale under static circumstances. d) V_{OC}, e) Q_{SC}, and f) I_{SC} versus time under dynamic circumstances.

Consequently, the electric potentials created by both charges cancel each other. Therefore, the output voltage in the steady state is much lower than that in the initial state. Finally, the output behavior under extremely high load resistance conditions is shown in Figure 3c. Remarkably, the output charge and current remained steady at zero, which is in accordance with the definition of the OC condition in which charge is not allowed to flow between the electrodes. However, the output voltage fluctuates drastically as the separation distance between the two tribomaterials periodically varies. The peak output voltage remains remarkably high and does not decay over time. This is because, as charge transfer is blocked, the electric potential is not neutralized. Therefore, this is a pure V_{OC} created only by the contact electrification charge. Notably, the peak voltage under OC conditions was higher than that in the steady state under finite high resistance conditions.

Additional information on the various loading conditions is presented in Figures S6 and S7 (Supporting Information). Figure S6 (Supporting Information) shows electrical output behavior under remarkably low resistance conditions, where 0 Ω, 50 Ω, and 10 MΩ were chosen as ideal SC conditions, the internal resistance of SR 570, and that of a standard oscilloscope, respectively. As shown in the Figure, except voltage under SC conditions, all exhibit the same tendencies. An identical waveform shape occurs repeatedly with no transient stage observed. Additionally, the output charge and current remain unchanged with the external load resistance, whereas the output voltage varies drastically as the resistance increased. Therefore, the existence of the resistor can be neglected when considering the output charge and current under low resistance conditions. Consequently, the experimental data on charge and current under low resistance conditions can be regarded as those under SC conditions.

Figure S7 (Supporting Information) displays electrical output characteristics under high resistance conditions, including 10 GΩ, 100 GΩ, and ∞ Ω. This figure shows two remarkable output trends. First, under high resistance conditions but OC conditions, the output charge saturates during the transient state and fluctuates around a specific value after the saturation. Meanwhile, the peak current and voltage attenuate exponentially during the transient state and converged to specific values in a steady state. Hence, we focused on the steady state rather than on the transient state. Second, the value of the peak current in the steady state decreases with the load resistance, eventually dropping to zero under OC conditions. Conversely, the value of the peak voltage in the steady state increases with the load resistance, ultimately reaching its maximum under OC conditions.

These trends are illustrated in Figure S8 (Supporting Information) in detail. Figure S8a (Supporting Information) shows the theoretical effect of resistance on the RMS current, voltage, and

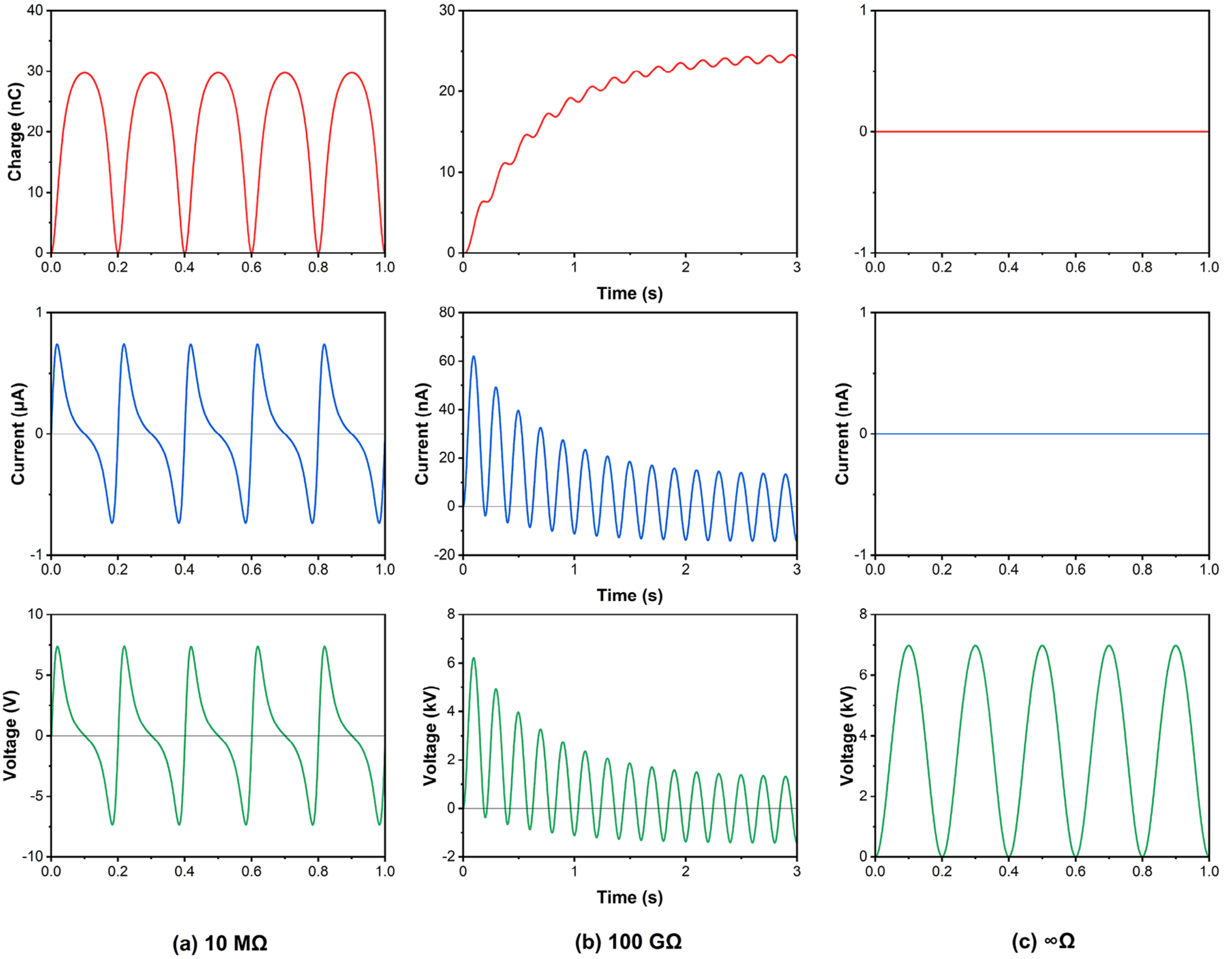

Figure 3. Predicted electrical output characteristics from the new theoretical model under different load resistance conditions. Simulated output charge, current, and voltage under various loading conditions, including a) 10 MΩ, b) 100 GΩ, and c) ∞ Ω.

power in the steady state. We simulated the RMS value, rather than the peak value, in comparison with the experimental results shown in Figure S8b (Supporting Information), where the RMS power is obtained by multiplying the RMS voltage by the RMS current. Theoretical simulation tells us that the plotted curves have three different regions: low resistance region ($R < 10^7$ Ω), high resistance region ($R > 10^{11}$ Ω), and middle resistance region (10^7 Ω $< R < 10^{11}$ Ω). In the first region, the output current remains high, whereas the output voltage is close to zero. This trend is reversed in the high resistance region, where the output current is close to zero while the output voltage remains high. In the other region, the middle resistance region, both the output current and voltage are transient. Remarkably, the maximum output power is observed at this stage. Otherwise, the output power remained almost zero. Figure S8b (Supporting Information) presents the results of an experimental investigation to validate these theoretical predictions. The experimentally observed current is in good agreement with the calculated current. The measured voltage shows a similar trend to the simulated one, but a discrepancy is observed in magnitude. Accordingly, recorded and predicted power are in discordance with each other in terms of magnitude. But they have a similar tendency of variation. Notably, they agree that the optimum resistance is $\approx 10^9 - 10^{10}$ Ω. This observation substantiates that the TENG has a considerably high internal impedance.

4.3. Parametric Studies Using the EQETD Model to Investigate the Electrical Output Characteristics under Different Circumstances

V_{OC} and I_{SC} provide the upper limits of the instantaneous voltage and current through the external circuit, which contributes to the generation of electrical power. Hence, they are core factors used for predicting electrical output performance and are dependent on many variables, such as driving conditions and device structure. Parametric studies were conducted experimentally and validated using the EQETD model to examine their effects on V_{OC} and I_{SC}. Furthermore, they are accompanied by a study on the behavior of Q_{SC} to better understand them. It is to be noted which

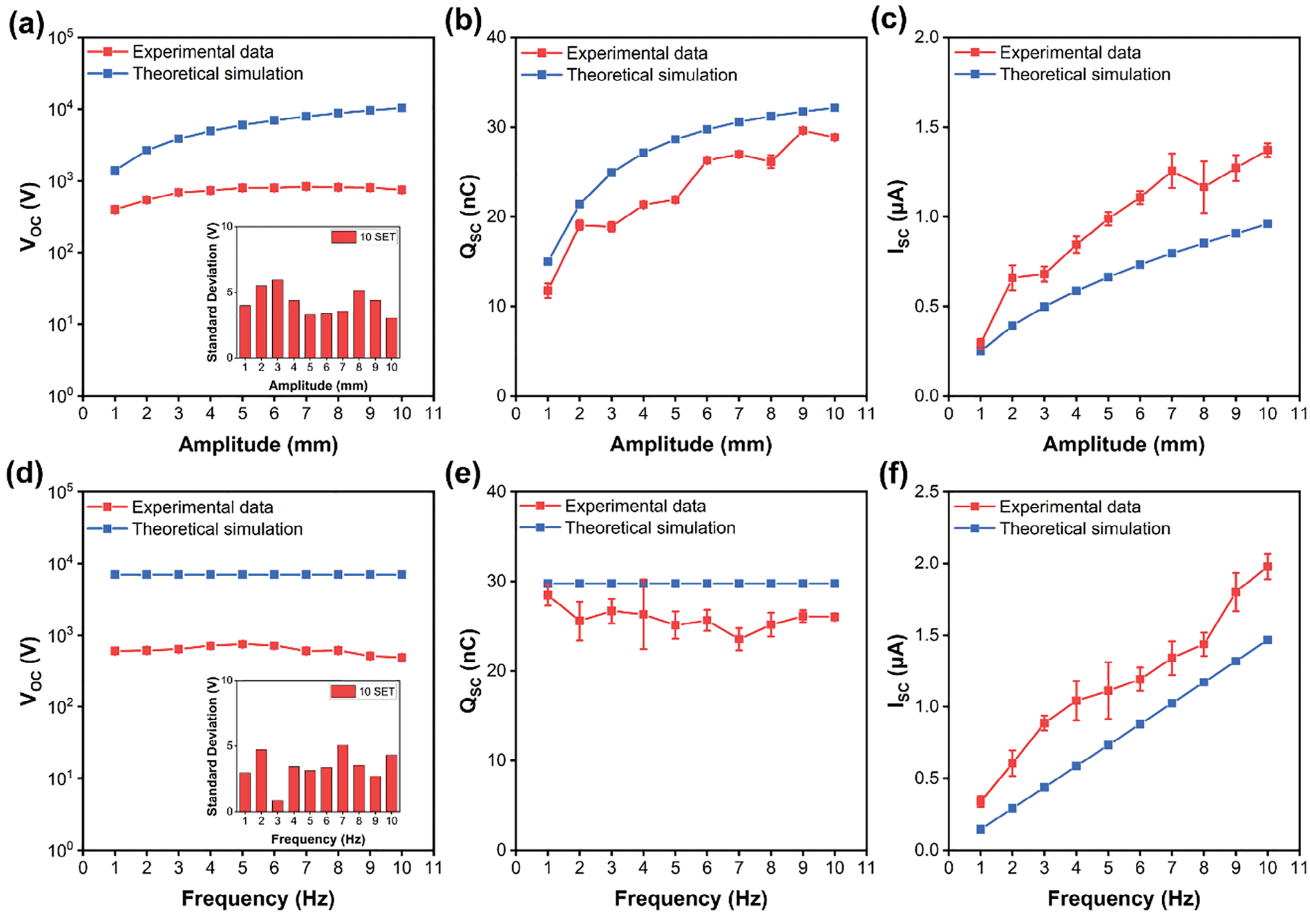

Figure 4. Theoretical and experimental peak voltage, charge, and current under different driving conditions such as amplitude and frequency. Peak a) V_{OC}, b) Q_{SC}, and c) I_{SC} versus amplitude. Peak d) V_{OC}, e) Q_{SC}, and f) I_{SC} versus frequency.

variables were selected to be explored and why those variables were chosen. For simplicity, we assumed that the plate is square, and two plates have the same dimensions and dielectric constant. The choice of the number of Gauss points in Equation (2) is explained by the Method section. According to Equation (13), the electrical output is expected to be proportional to the contact electrification charge density. Thus, this simple exploration was excluded from the study. The effect of the resistance on the electrical output was already investigated in preceding section. Consequently, the remaining variables are the area, thickness, and dielectric constant of the plates, as well as the amplitude and frequency of the mechanical input. Even though analyzing the dielectric constant dependence of the electrical output is valuable, the experimental validation of that is relatively difficult compared to other parametric studies. Therefore, we investigated the effects of four variables on the output: amplitude, frequency, thickness, and area.

Figure 4 shows the peak V_{OC}, Q_{SC}, and I_{SC} variations with the driving conditions, including the amplitude and frequency of the mechanical movements of the TENG layer. Setting frequency as 5 Hz, amplitude dependence of output was investigated, as shown in Figure 4a–c. All outputs increased with amplitude, accompanied by a decreasing gradient. The tendencies of V_{OC} and Q_{SC} are shown in Figure 4a,b. The declining gradient of V_{OC} can be explained by the DDEF concept, whose magnitude decays with the separation distance. Thus, the V_{OC} which is evaluated by the line integral of the electric field, converges to a specific value as the distance increases infinitely. This was validated experimentally. Similarly, Q_{SC} increases with amplitude until it eventually plateaus. Because Q_{SC} is defined as the charge transferred to neutralize V_{OC}, it is expected that they will show similar trends. The experimental results support this assumption. As the amplitude increased, Q_{SC} as well as I_{SC} elevate, which is defined as the derivative of Q_{SC} with respect to time. This prediction was not surprising and was in good agreement with the experimental results.

Maintaining an amplitude 6 mm, the effect of frequency on the output was obtained, as shown in Figure 4d–f. The theoretical model predicts that V_{OC} and Q_{SC} are constant with respect to the frequency. The explanation for these tendencies can be described as follows: V_{OC} and Q_{SC} are not electrodynamic characteristics affected by frequency but electrostatic characteristics dependent on the static charge and system geometry. The experimental tendency of V_{OC} and Q_{SC} agrees well with the theoretical prediction. Unlike the two former cases, I_{SC} is affected by dynamic conditions, including frequency, because it is defined as the transferred charge per unit of time. Although Q_{SC} is unchanged, increasing the frequency shortens the time required for charge

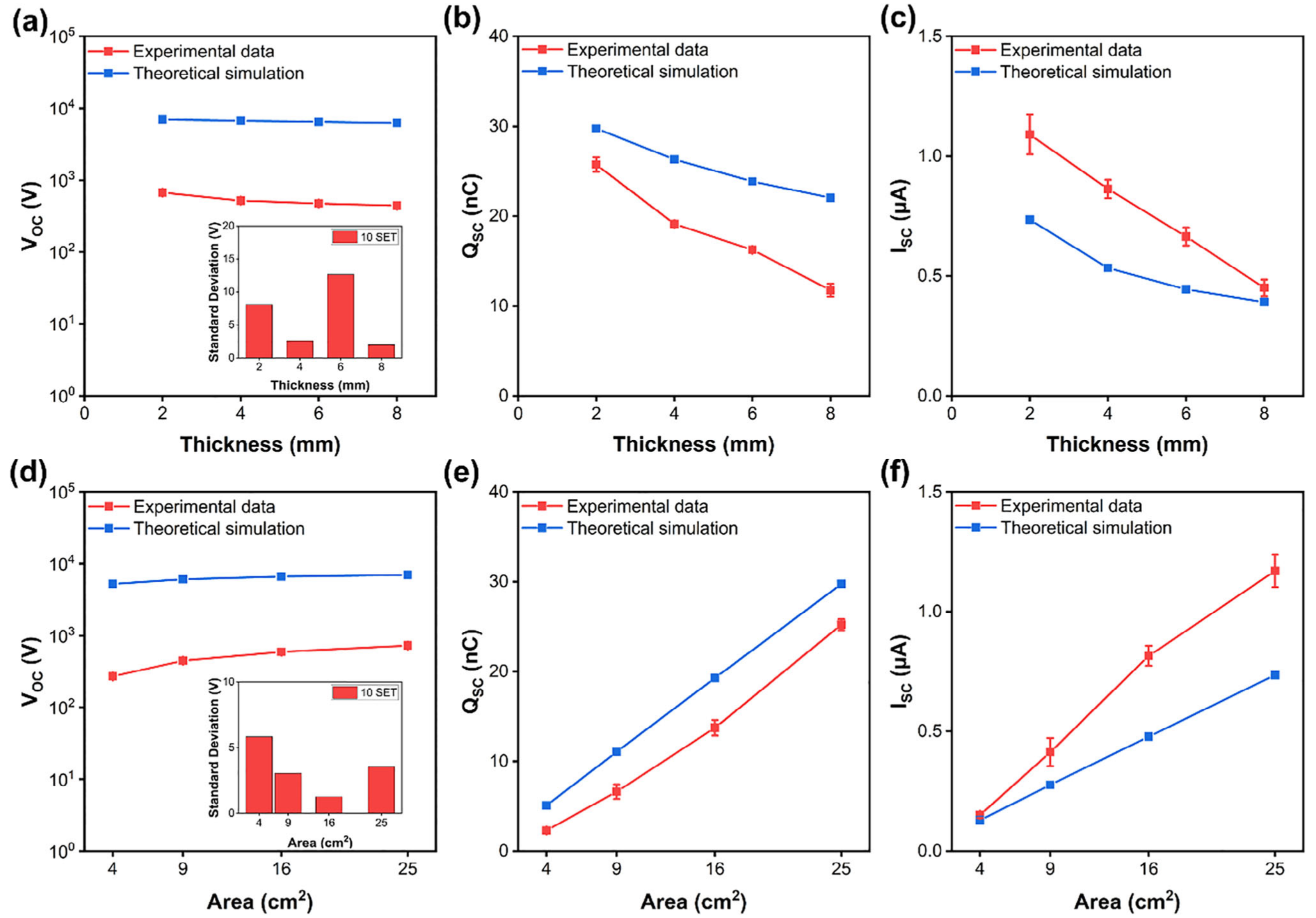

Figure 5. Theoretical and experimental peak voltage, charge, and current under different device dimensions, including plate thickness and area. Peak a) V_{OC}, b) Q_{SC}, and c) I_{SC} versus plate thickness. Peak d) V_{OC}, e) Q_{SC}, and f) I_{SC} versus plate area.

transfer. Consequently, the proportionality between I_{SC} and frequency is predicted theoretically. The experimental results are in accordance with this rule.

Device structures and driving conditions are parameters that affect the electrical output characteristics. **Figure 5** presents the results of this parametric study. The effects of the substrate thickness on the peak V_{OC}, Q_{SC}, and I_{SC} are shown in Figure 5a–c. The theoretical model predicts that V_{OC} decreases slightly with the thickness. This tendency is explained through the DDEF concept as follows. V_{OC} is composed of three parts, which are expressed in the mathematical formula as follows:

$$V_{OC} = V_{d_1} + V_z + V_{d_2} \tag{16}$$

where V_{d_1}, V_z, and V_{d_2} represent the electric potential differences between opposite sides of dielectric 1, between two tribolayers, and between opposite sides of dielectric 2, respectively (see Figure S1a, Supporting Information for a graphical representation). If the separation distance z is constant, V_z also becomes constant. Then, V_{OC} changes only by V_{d_1} and V_{d_2}, which are functions of the thicknesses of dielectrics 1 and 2, respectively. Because the magnitudes of V_{d_1} and V_{d_2} increase with the dielectric thickness, and their signs are opposite to the sign of V_z, their total summation, which is equal to V_{OC} diminishes with the dielectric thickness. Experimental observations support this inference. Likewise, Q_{SC} and I_{SC} showed similar trends to V_{OC}. The reason for the decrease Q_{SC} with increasing thickness is the amount of charge that needs to be transferred to neutralize V_{OC} decline as thickness increases. For similar reasons, as the thickness increases, I_{SC} decreases which is the transferred charge per unit time. These predictions were validated experimentally.

Substrate area is another parameter that defines the device structure. Figure 5d–f shows the area dependence of the peak V_{OC}, Q_{SC}, and I_{SC}. All outputs were enhanced as the area increased. These tendencies can be inferred from the DDEF concept, which considers the finite size of charged plates. Imagine the following two extreme cases: First, if the area of the tribolayers becomes zero, holding the contact electrification charge density constant, V_{OC} falls to zero. Conversely, if the area increases infinitely, the electric field becomes uniform, and the CA model can be employed. Subsequently, V_{OC} approached a certain value. Considering the arbitrary case between the two cases treated above, it is natural that V_{OC} increases with the area. Experimental data validates this inference. Q_{SC} and I_{SC} were predicted to be proportional to the area. As the area increases, V_{OC} increases, but the increment is insignificant. Therefore, area can be regarded as a single factor affecting Q_{SC} and I_{SC} neglecting the change in V_{OC}. To neutralize a constant V_{OC}, the induced charge density must reach a certain level. Because the charge is evaluated as the product of charge density and area, the charge is proportional to the area, holding the charge density constant. Additionally, as the area increases, an elevated Q_{SC} enhances I_{SC}. Experimental observations validate these inferences.

Energy conversion efficiency is an important parameter to be considered. We simulated efficiency through Equation (14) under diverse parametric conditions. Figure S9 (Supporting Information) shows the effects of amplitude, frequency, thickness, area, and external resistance on efficiency. Remarkably, efficiency goes up and down as resistance increases. This phenomenon accords with the resistance dependence of electrical power output as studied in Figure S8 (Supporting Information). The relationship between efficiency and other parameters is numerically displayed in the Figure, but their essential trends and underlying reasons are beyond the scope of this paper.

We investigated the effects of diverse variables on the output characteristics, but the observed trends were monotonically either increased or decreased with respect to parameters excluding resistance. Thus, the optimized parameters for the highest output performance were not able to be found in these studies even though both theoretical and experimental explorations were conducted. However, we believe that this model can be utilized to conduct optimization for the output performance with be assisted by sophisticated optimization techniques such as Gradient Descent.

4.4. Comparison with Existing Models

To validate the derived model, theoretical predictions from all models, including existing models and the derived model, were compared with the experimental observations. It is common practice to evaluate the effects of separation distance on V_{OC} to validate the proposed model. However, there is a significant difference between the simulated and experimental results.[23,24] We estimated that this discrepancy is attributed to the use of the analysis method. Theoretically, V_{OC} are evaluated by preventing charge transfer between electrodes. However, the experimentally measured voltage is always lower than theoretical one because the OC concept cannot be realized in practice. Hence, we simulated the electrical behavior of the TENG under realistic conditions instead of under ideal circumstances.

First, the experimental voltage was obtained in the same way as described above. The TENG system was subjected to sinusoidal movement to contact and separate the triboi nterfaces periodically. The experimental conditions were kept constant, as listed in Table S1 (Supporting Information), while the mechanical excitation amplitude was varied from 1 mm to 10 mm. The separation distance varies as a function of time, and the maximum peak of that is called the amplitude. Electrical measurement was conducted by an oscilloscope, which has an internal resistance of 10 MΩ. Second, a simulation was performed to closely replicate the experimental conditions. Theoretical voltage was evaluated by assuming that the TENG was mechanically excited periodically and was connected through the electrical load resistance of 10 MΩ. Based on the conditions mentioned above, theoretical simulations were conducted for each model, where σ_t was set to 13.9 μC m^{-2} in common.

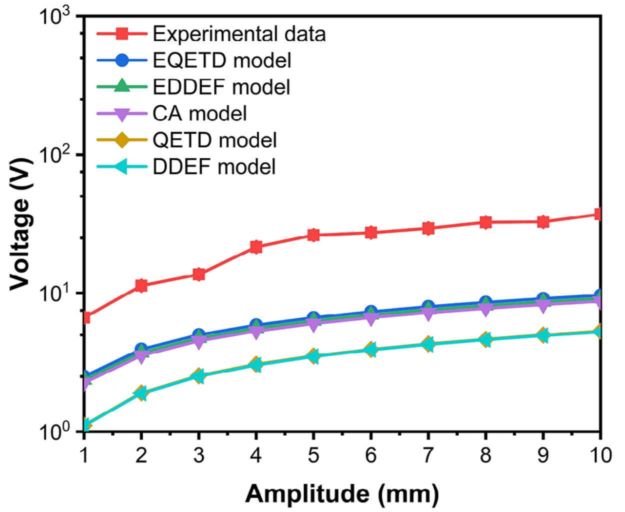

Figure 6. Comparison between observed and predicted output voltage trends under load resistance condition of 10 MΩ. Theoretical predictions from existing and current models (EQETD model, EDDEF model, CA model, QETD model, and DDEF model) were obtained. Experimental results were compared to them. The figure shows that the EQETD model provides the closest approximation to experimental data.

Figure 6 shows a comparison between experimental measurements and theoretical predictions from different models of the peak voltage as a function of amplitude. All showed the same trend. As the amplitude increases, the output voltage increases, whereas its gradient diminishes. The only difference between them is their vertical positions. Although all models exhibited similar trends to the experimental data, EQETD model provided the closest predictions. Figure S10 (Supporting Information) is another result comparing the voltage measured and calculated by all models under load resistance conditions of 1 MΩ. Unlike the former case, the current across the resistance is measured by SR 570 and the voltage across the resistance is calculated using Ohm's law. The comparison result in this case also shows that the EQETD model provides the closest predictions to experimental data. Therefore, we conclude that the EQETD model is the most enhanced quasi–electrostatic model.

5. Conclusion

A new theoretical model for the VCS–TENG is proposed, named the enhanced quasi–electrostatic 3D (EQETD) charge model. A concise review of previously published models of VCS–TENG is presented. The limitations of existing models and the reasons for their inaccuracies are discussed in detail. To address these issues, the mathematical derivation processes proposed for each model were integrated. In particular, the formula used to evaluate the voltage was corrected. The derivation involves multiple integrals that are challenging to compute. To simplify the problem, mathematical techniques were used; consequently, multiple integrals were reduced to a summation of double integrals. All processes of deriving the formulae are described in detail. Experiments validated the proposed model. First, the contact electrification charge density due to friction between the tribomaterials was determined using the least squares method. Theoretical predictions were obtained using the calculated charge density and compared with the experimental data. Although there were some deviations between the theoretical simulations and experimental observations, their tendencies were in accordance. A comparison between the experimental observations and theoretical predictions from each model indicates that the EQETD model provides the closest results to the experimental data among the existing models. Therefore, we conclude that the EQETD model is the most advanced quasi–electrostatic model. We expect this model to provide a theoretical understanding, forecast electrical output characteristics, and optimize the design of VCS–TENG in the future.

6. Experimental Section

Fabrication of TENG for Experiments: To verify the new theoretical model, a series of experiments were conducted on TENG structures, as shown in Figure 1a. A schematic illustration of the dielectric–dielectric VCS–TENG used for the experiments is shown in Figure S11 (Supporting Information). As shown in the Figure, PMMA was selected as the substrate of the TENG, to which the Al electrode and tribomaterials were attached. Nylon and Polytetrafluoroethylene (PTFE) were selected as positive and negative tribomaterials, respectively. The geometric dimensions of the device structure are listed in Table S1 (Supporting Information). These values were used throughout the experiments unless specified otherwise. To experimentally investigate the effect of the substrate thickness on the electrical output, TENGs with different thicknesses were fabricated by laminating multiple PMMA slices of the same thickness of 2 mm.

Tribo–Charging Method: To obtain an experimental output in a steady state for the TENG system, it is necessary to saturate the static charges on the tribomaterials of the TENG. Therefore, an extra PTFE slice was rubbed onto the fur and charged. Subsequently, the charged PTFE slices and fur were rubbed against the Nylon and PTFE layers of the TENG to supply the generated triboelectric charge. Finally, the tribolayers were subjected to sinusoidal movement through shakers, which represented periodic contact and separation between the triboInterfaces. All the mechanical triggering parameters are listed in Table S1 (Supporting Information), which continues throughout the experiments unless specified otherwise.

Measurement of Electrical Output: To validate the proposed model, experimental measurements for electrical signals such as current and voltage were conducted. Throughout the study, the experiments conducted can be classified into three categories: I_{SC}, V_{OC}, and current and voltage under practical conditions. Frist, I_{SC} was measured using SR 570, which was connected to the TENG in series. Since SR 570 has an internal resistance as low as of 50 Ω, the output current is almost same to that under ideal SC condition as explored in Figure S6 (Supporting Information). Second, V_{OC} was calculated using Ohm's law and the measured current flowing through a significantly high external resistance. Current was measured using SR 570, which was connected to the TENG and resistance of 10 GΩ in series. Third, current flowing through a common resistance was measured using SR 570, which was connected to the TENG and resistance in series. Voltage across the common resistance was calculated using Ohm's law and measured current flowing through the resistance. In special cases where the voltage across the resistance of 10 MΩ is of interest, such as Figure 6, the voltage was directly measured using oscilloscope because it has an internal resistance of 10 MΩ.

Numerical Processing of Experimental Data: The experimental data were analyzed numerically to establish underlying trends. The measured positive and absolute negative peaks were averaged to determine the magnitudes of the raw signal peaks. Additionally, the accumulated charge was evaluated by integrating the sampled current data with respect to time. Measured current and calculated charge under SC condition were compared with simulated predictions to determine contact electrification charge density σ_t through the least squares method. As shown in Figure S12 (Supporting Information), it can be concluded that 13.9 μC m^{-2} of σ_t resulted in the smallest squared percentage error between the experimental and simulated data. Hence, σ_t was set as 13.9 μC m^{-2} in all the following simulations.

Preset of a User–Defined Parameter for Simulation: When evaluating the value of the function in Equation (2), it was necessary to preset the value of n, which is the number of Gauss points belonging to the interval of integration. In this study, the value of n was set to 6. Notably, this new EQETD model would reduce the previous EDDEF model if n is set to 1.

Supporting Information

Supporting Information is available from the Wiley Online Library or from the author.

Acknowledgements

This work was supported by a National Research Foundation of Korea (NRF) grant funded by the Korean Government (MSIT) (No. RS–2023–00210363).

Conflict of Interest

The authors declare no conflict of interest.

Author Contributions

S.K. performed conceptualization, methodology, validation, formal analysis, and investigation, wrote the original draft, wrote the review, and performed editing, and visualization. J.–W.H. performed methodology, validation, supervision, and wrote the review, and performed editing. J.C. performed conceptualization, methodology, validation, and supervision, wrote the original draft, wrote the review and editing, and performed visualization.

Data Availability Statement

The data that support the findings of this study are available from the corresponding author upon reasonable request.

Keywords

energy harvesting, triboelectric nanogenerator, theoretical model

Received: February 25, 2025
Revised: April 1, 2025
Published online:

[1] D. Maystre, *Compt. Rend. Physiq.* **2014**, *15*, 387.
[2] F. Fan, Z. Tian, Z. L. Wang, *Nano Energy.* **2012**, *1*, 328.
[3] C. Wu, A. C. Wang, W. Ding, H. Guo, Z. L. Wang, *Adv. Energy Mater.* **2019**, *9*, 1802906.
[4] H. Yoon, D. Kim, W. Seung, U. Khan, T. Y. Kim, T. Kim, S. Kim, *Nano Energy* **2019**, *63*, 103857.
[5] F. Wang, M. Li, B. Wang, J. Zhang, Y. Cheng, L. Liu, F. Lv, S. Wang, *Sci. Rep.* **2015**, *5*, 7617.

[6] M. Kim, M. Kim, H. Kwon, S. Jo, Y. Kim, *RSC Adv.* **2017**, *7*, 48368.
[7] I. Tcho, S. Jeon, S. Park, W. Kim, I. K. Jin, J. Han, D. Kim, Y. Choi, *Nano Energy* **2018**, *50*, 489.
[8] X. Yang, L. Xu, P. Lin, W. Zhong, Y. Bai, J. Luo, J. Chen, Z. L. Wang, *Nano Energy* **2019**, *60*, 404.
[9] P. Yin, K. C. Aw, X. Jiang, C. Xin, H. Guo, L. Tang, Y. Peng, Z. Li, *Nano Energy.* **2022**, *95*, 106976.
[10] S. Potu, R. K. Rajaboina, B. Gollapelli, J. Vallamkondu, S. Mishra, H. Divi, A. Babu, U. Kumar, P. Kodali, *ACS Appl. Energy Mater.* **2022**, *5*, 13702.
[11] C. Cao, Z. Li, F. Shen, Q. Zhang, Y. Gong, H. Guo, Y. Peng, Z. L. Wang, *Energy Environ. Sci.* **2024**, *17*, 885.
[12] C. Le, T. Nguyen, D. Vu, C. Vo, K. K. Ahn, *Mater. Today Sustainability* **2022**, *19*, 100158.
[13] M. Li, Y. Lou, J. Hu, W. Cui, L. Chen, A. Yu, J. Zhai, *Small* **2024**, *20*, 2402009.
[14] J. Zhang, P. Chen, L. Zu, J. Yang, Y. Sun, H. Li, B. Chen, Z. L. Wang, *Small* **2022**, *18*, 2202835.
[15] W. Ding, J. Zhou, J. Cheng, Z. Wang, H. Guo, C. Wu, S. Xu, Z. Wu, X. Xie, Z. L. Wang, *Adv. Energy Mater.* **2019**, *9*, 1901320.
[16] Z. Lin, C. Sun, G. Zhang, E. Fan, Z. Zhou, Z. Shen, J. Yang, M. Liu, Y. Xia, S. Si, *Nano Res.* **2022**, *15*, 7484.
[17] Y. Lai, J. Deng, S. Niu, W. Peng, C. Wu, R. Liu, Z. Wen, Z. L. Wang, *Adv. Mater.* **2016**, *28*, 10024.
[18] W. Sun, Z. Ding, Z. Qin, F. Chu, Q. Han, *Nano Energy* **2020**, *70*, 104526.
[19] H. Kim, H. J. Hwang, N. D. Huynh, K. D. Pham, K. Choi, D. Ahn, D. Choi, *Research* **2021**, *2021*, 6426130.
[20] Y. Wang, X. Liu, T. Chen, H. Wang, C. Zhu, H. Yu, L. Song, X. Pan, J. Mi, C. Lee, *Nano Energy* **2021**, *90*, 106503.
[21] D. Choi, Y. Lee, Z. Lin, S. Cho, M. Kim, C. K. Ao, S. Soh, C. Sohn, C. K. Jeong, J. Lee, *ACS Nano* **2023**, *17*, 11087.
[22] S. Niu, S. Wang, L. Lin, Y. Liu, Y. S. Zhou, Y. Hu, Z. L. Wang, *Energy Environ. Sci.* **2013**, *6*, 3576.
[23] R. D. I. G. Dharmasena, K. Jayawardena, C. A. Mills, J. Deane, J. V. Anguita, R. A. Dorey, S. Silva, *Energy Environ. Sci.* **2017**, *10*, 1801.
[24] X. Chen, F. Zhang, C. Han, Y. Liu, G. Y. Chen, X. Sun, Z. Wen, *Nano Energy* **2023**, *111*, 108435.
[25] A. A. Ahmed, H. M. Abdullah, T. F. Qahtan, A. G. Muthalif, M. Nafea, M. S. M. Ali, *Nano Energy* **2023**, *117*, 108836.
[26] D. J. Griffiths, *Introduction to electrodynamics*, Cambridge University Press, Cambridge, England **2023**.
[27] S. Chapra, *EBOOK: Applied Numerical Methods with MATLAB for Engineers and Scientists*, McGraw Hill, New York, USA **2011**.
[28] H. Zhang, L. Yao, L. Quan, X. Zheng, *Nanotechnol. Rev.* **2020**, *9*, 610.
[29] H. Zhao, H. Wang, H. Yu, Q. Xu, X. Li, J. Guo, J. Shao, Z. L. Wang, M. Xu, W. Ding, *Energy Environ. Sci.* **2024**, *17*, 2228.
[30] X. Cui, Y. Zhang, G. Hu, L. Zhang, Y. Zhang, *Nano Energy* **2020**, *70*, 104513.
[31] M. N. Haque, G. Shanmugam, J. Joseph, S. Karakkad, *2024 IEEE 5th International Conference on Dielectrics (ICD)*, IEEE, Piscataway, NJ **2024**.
[32] C. Jiang, K. Dai, F. Yi, Y. Han, X. Wang, Z. You, *Nano Energy.* **2018**, *53*, 706.
[33] R. Zhang, H. Olin, *EcoMat* **2020**, *2*, 12062.
[34] J. Shao, M. Willatzen, Y. Shi, Z. L. Wang, *Nano Energy* **2019**, *60*, 630.
[35] R. I. G. Dharmasena, J. H. Deane, S. R. P. Silva, *Adv. Energy Mater.* **2018**, *8*, 1802190.
[36] S. Niu, Y. Liu, S. Wang, L. Lin, Y. S. Zhou, Y. Hu, Z. L. Wang, *Adv. Mater.* **2013**, *25*, 6184.
[37] S. Niu, Y. Liu, X. Chen, S. Wang, Y. S. Zhou, L. Lin, Y. Xie, Z. L. Wang, *Nano Energy* **2015**, *12*, 760.
[38] S. Niu, Y. Liu, S. Wang, L. Lin, Y. S. Zhou, Y. Hu, Z. L. Wang, *Adv. Funct. Mater.* **2014**, *24*, 3332.
[39] G. Xu, X. Li, X. Xia, J. Fu, W. Ding, Y. Zi, *Nano Energy* **2019**, *59*, 154.